Journal of Materials Chemistry C

PAPER

View Article Online
View Journal | View Issue

Cite this: J. Mater. Chem. C, 2018, 6, 6714

Controllable two-dimensional luminescence tuning in Eu^{2+},Mn^{2+} doped $(Ca,Sr)_9Sc(PO_4)_7$ based on crystal field regulation and energy transfer†

Sisi Liang,[ab] Peipei Dang,[ab] Guogang Li,*[c] Maxim S. Molokeev,[d] Yi Wei,[ab] Yi Wei,[c] Hongzhou Lian,[a] Mengmeng Shang,[e] Abdulaziz A. Al Kheraif[f] and Jun Lin*[ag]

Received 17th April 2018,
Accepted 31st May 2018

DOI: 10.1039/c8tc01825a

rsc.li/materials-c

Currently, controllable luminescence tuning and the generation of single component white emission are viable strategies to modify and optimize the luminescence performances of phosphors, which offer appealing prospects for the w-LED lighting industry. In this paper, we designed two-dimensional (2D) tunable color coordinates on the CIE diagram in the Eu^{2+},Mn^{2+} doped $(Ca,Sr)_{9x}Sc(PO_4)_7$ system by a combination of crystal field regulation and the energy transfer method. X-ray powder diffraction (XRD) and Rietveld refinement were utilized to analyze the phase composition and structural variation of the studied phosphors. The transmission electron microscopy (TEM) and photoluminescence spectra were exploited to analyze the generation of nanosegregation. The effects of the schedule of cation substitutions and energy transfer on the photoluminescence properties were investigated in detail. The corresponding luminescence mechanisms of the red-shifted emission with $Sr^{2+} \rightarrow Ca^{2+}$ substitution and $Eu^{2+} \rightarrow Mn^{2+}$ energy transfer were deeply discussed and proposed. In addition, the temperature-dependent thermal quenching behavior and the electroluminescence (EL) performance of the fabricated w-LED devices were also investigated to characterize the prepared $Ca_{9(1-0.03-x-y)}Sr_{9x}Sc(PO_4)_7$:0.27$Eu^{2+}$,9y$Mn^{2+}$. Finally, a representative w-LED device composed of a 369 nm UV chip and $Ca_{9(1-0.03-0.02-0.5)}Sr_{4.5}Sc(PO_4)_7$:0.27$Eu^{2+}$,0.18$Mn^{2+}$ could present excellent EL performance with the parameters CRI = 88, CCT = 3122 K and color coordinate (0.45, 0.44), which could well meet the commercial standard of warm white light. Therefore, our results suggest that this two-step luminescence tuning method is feasible to be applied in other phosphor systems for obtaining efficient white emitting phosphors.

1. Introduction

In view of the ever-increasing energy crisis problems and the broadband emitting yellow phosphor and environmental concerns, it is imperative to develop a high-efficiency lighting source to reduce energy consumption and pollution. As lighting is an essential part of human life, a breakthrough in the lighting sources field, ranging from displays to solid-state lighting, is urgently needed to keep up with the pace of social progress. The requirement of lighting development has been emphasized, and lighting technology is crucial to fulfilling the international energy saving ambitions.[1–12] To date, most commercially available phosphor-converted white light-emitting diodes (w-LEDs) in the lighting sources field are based on the broadband emitting yellow phosphor $Y_3Al_5O_{12}$:Ce^{3+} (usually YAG:Ce^{3+}) and an InGaN-based blue-emitting LED chip.[13] However, a prerequisite for further commercialization and promotion of w-LEDs demands that some major shortcomings be overcome, such as their high color temperature (CCT, >6000 K) and low color rendering index (CRI, Ra < 80). On one hand, it is well known that cool white light is harmful to the vision health of people. Meanwhile, some experts have verified that the blue light from w-LEDs can suppress the production of melatonin in the human brain,[14,15] which has a pernicious effect on sleep quality. On the other hand, in order to cover the deficiency of

[a] State Key Laboratory of Rare Earth Resource Utilization, Changchun Institute of Applied Chemistry, Chinese Academy of Sciences, Changchun 130022, P. R. China. E-mail: jlin@ciac.ac.cn; Fax: +86-431-85698041; Tel: +86-431-85262031
[b] University of Sciences and Technology of China, Hefei 230026, P. R. China
[c] Engineering Research Center of Nano-Geomaterials of Ministry of Education, Faculty of Materials Science and Chemistry, China University of Geosciences, 388 Lumo Road, Wuhan 430074, P. R. China
[d] Laboratory of Crystal Physics, Kirensky Institute of Physics, SB RAS, Krasnoyarsk 660036, Russia
[e] School of Chemistry and Chemical Engineering, Qingdao University, Qingdao 266071, P. R. China
[f] Dental Health Department, College of Applied Medical Sciences, King Saud University, Riyadh, Saudi Arabia. E-mail: aalkhuraif@ksu.edu.sa
[g] School of Applied Physics and Materials, Wuyi University, Jiangmen, Guangdong, 529020, P. R. China

† Electronic supplementary information (ESI) available. See DOI: 10.1039/c8tc01825a

emission in the red region of w-LEDs,[16] some researchers have reported the method of adding an additional red phosphor into the composition of w-LEDs.[16] This method could increase the CCT of the w-LED, but another problem will emerge in this system. Besides the increase in cost, the reabsorption and uncontrollable color balance between the different phosphors will lead to an insurmountable difficulty in the fabrication of the w-LEDs.

To solve the problems mentioned above, the synthesis of an efficient single-component white-emitting phosphor is a viable strategy. Among various ways to realize single-component white-emitting emission, researchers have commonly devoted their attention to facile energy transfer.[17–21] However, energy transfer between several rare-earth (RE) ions or the combination of multi-emission from different RE ions can only adjust the emission colors linearly in one-dimension on the CIE (Commission Internationale de L'Eclairage) diagram.[22–24] This limits the achievement of more ideal luminescence properties, such as better CCTs and color coordinates. In order to overcome the above drawbacks, Xia's group[25,26] reported a single-doped white phosphor that was synthesized by a two-step method.[27] Through the combination of controlling the chemical composition of the solid solution host matrix and the valence state of the single Eu dopant, they successfully designed a white-emitting phosphor, $Na_4CaMgSc_4Si_{10}O_{30}$:Eu, with excellent color rendering index. These two steps mean that the chromaticity coordinates of the phosphors can move linearly along different paths on the CIE diagram. Consequently, two-dimensional tuning of the color coordinates has been achieved, which allows more flexible tuning to obtain the optimum luminescence properties.

Inspired by the above work, while also considering the complex and unmanageable valence states of RE ions in phosphor compounds, we designed a two-step method that combines crystal field regulation and energy transfer to realize the single-component white-emitting phosphor $Ca_{9(1-0.03-x-y)}Sr_{9x}Sc(PO_4)_7$:$0.27Eu^{2+}$, $9yMn^{2+}$. This study achieved the two-dimensional tuning of the chromaticity coordinates, and the as-prepared phosphors have been fabricated as w-LEDs by simply combining them with a UV chip. The characterization of the structural variation and the photoluminescence properties are discussed in detail, and the possible luminescence red-shift mechanisms and nano-segregation phenomenon are proposed. The results indicate that the studied $Ca_{9(1-0.03-x-y)}Sr_{9x}Sc(PO_4)_7$:$0.27Eu^{2+}$,$9yMn^{2+}$ is a promising phosphor and this method has the potential to be utilized in other phosphor systems.

2. Experimental section

2.1 Materials and preparation

A series of phosphors with the nominal compositions of $Ca_{9(1-0.03-x)}Sr_{9x}Sc(PO_4)_7$:$0.27Eu^{2+}$ (abbreviated as CSSPO:Eu^{2+}) and $Ca_{9(1-0.03-x-y)}Sr_{9x}Sc(PO_4)_7$:$0.27Eu^{2+}$,$9yMn^{2+}$ (abbreviated as CSSPO:Eu^{2+},Mn^{2+}) were synthesized by a conventional solid-state reaction at high temperature. All of the reagents in this experiment, $CaCO_3$ (99.99%), $SrCO_3$ (A.R.), Sc_2O_3 (99.99%), $NH_4H_2PO_4$ (A.R.), $MnCO_3$ (A.R.), and Eu_2O_3 (99.99%), were used directly without any further purification. The typical synthesis process is described as follows: stoichiometric amounts of the raw materials were weighed, and mixed in an agate mortar and ground homogeneously for 30 min, adding ethanol as the dispersing medium. Then, the mixture was dried in a baking box at 80 °C and the dried precursors were obtained. After grinding again, the obtained powder was transferred to a crucible and placed in a tube furnace, carrying out a sintering procedure at 1300 °C for 6 h under a reducing atmosphere of N_2–H_2 (90–10%). After firing, the samples were cooled to room temperature and ground again to obtain the resulting phosphor samples for further characterization.

LED fabrication. Phosphor-converted w-LED solid-state lighting devices were fabricated by combining the as-prepared $Ca_{9(1-0.03-x-y)}Sr_{9x}Sc(PO_4)_7$:$0.27Eu^{2+}$,$9yMn^{2+}$ phosphor and a 370 nm UV-chip. In a typical fabrication process, epoxy resins A and B were weighed with a ratio of 1 : 1, and then the appropriate amount of CSSPO:Eu^{2+},Mn^{2+} white phosphor was added. After thoroughly mixing, the obtained mixture was smoothly coated on the surface of an InGaN chip, and cured on the LED chip by heating at 150 °C for 1 h. After the packaging was completed, the optical properties of the w-LED devices were measured in an integrating sphere under a forward current of 20 mA.

2.2 Characterization

X-ray powder diffraction data of the $Ca_{9(1-x)}Sr_{9x}Sc(PO_4)_7$:$Eu^{2+}$ samples for Rietveld analysis were collected at room temperature with a Bruker D8 ADVANCE powder diffractometer (Cu-Kα radiation) and linear VANTEC detector. The step size of 2θ was 0.02°, and the counting time was 1 s per step with Cu-Kα radiation (λ = 0.15405 nm) in the range of 2θ from 10° to 100°. Rietveld refinement was performed by using TOPAS,[28] and the schematic diagram of the crystal structure was obtained using the VESTA program. Transmission electron microscopy (TEM) was performed with FEI Tecnai G2S-Twin microscope with a field-emission gun operating at 300 kV, and the images were obtained digitally with a Gatan multipole CCD camera. Photoluminescence excitation (PLE) and photoluminescence emission spectra (PL) were recorded on a Hitachi F-7000 spectrophotometer equipped with a 150 W xenon lamp as the excitation source. The lifetimes were analyzed with a Lecroy Wave Runner 6100 digital oscilloscope (1 GHz) using a tunable laser (pulse width = 4 ns, gate = 50 ns) as the excitation source (Continuum Sunlite OPO). The performances of the w-LEDs were measured by Starspec SSP6612. All of these measurements were carried out at room temperature. The temperature-dependent (0–200 °C) PL spectra were recorded on a fluorescence spectrophotometer equipped with a 450 W xenon lamp as the excitation source (Edinburgh Instruments FLSP-920) with a temperature controller.

3. Results and discussion

3.1 Phase identification and crystal structure analysis

Fig. 1 shows the XRD patterns of the CSSPO:xEu^{2+} (x = 0–1) samples and the standard JCPDS data no. 50-0340 of $Ca_9Sc(PO_4)_7$.[29]

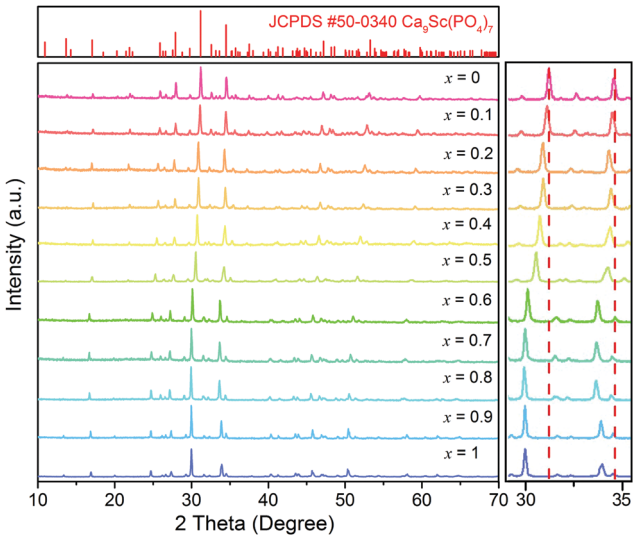

Fig. 1 The standard card (JCPDS no. 50-0340) data and the XRD patterns of the phosphors CSSPO:Eu^{2+} (x = 0–1).

Obviously, all of the diffraction patterns are in good agreement with the standard card information, suggesting that the cation substitution and the doping of Eu^{2+} retains the phase purity. Moreover, Eu^{2+} ions are homogeneously doped in the host lattice. It is noticed that all of the XRD diffraction peaks of the CSSPO:Eu^{2+} samples continuously shift towards to lower angle compared with that of CSPO:Eu^{2+}, indicating lattice expansion with the replacement of Sr^{2+} for Ca^{2+}.[11] This is reasonable due to the larger ionic radius of Sr^{2+} ions than Ca^{2+} ions ($r_{Ca^{2+}}$ = 1.00 Å, $r_{Sr^{2+}}$ = 1.18 Å). Regarding the reason for the phase purity with complete substitution, we infer that it is attributed to the contribution of nanosegregation, as will be discussed in the sections on photoluminescence properties.

To further accurately determine the phase purity and crystal structure, Rietveld refinement was performed by using TOPAS 4.2 for the CSSPO:Eu^{2+} samples with different Sr^{2+} substitution amounts. According to the refinement results, almost all of peaks of the studied samples are indexed to rhombohedral cells (*R3c*) with parameters close to $Ca_9In(PO_4)_7$ (the garnet-type structure in the Inorganic Crystal Structure Database #59590) besides small impurity peaks of Sc_2O_3 and $Sr_3(PO_4)_2$.[28,30] Therefore, $Ca_9In(PO_4)_7$ was taken as the starting model for Rietveld refinement. The sites of Ca^{2+} ions were occupied by Ca^{2+}/Sr^{2+} ions with fixed occupations according to the suggested chemical formula. The sites of In^{3+} ions were occupied by Sc^{3+} ions. The refinements were stable and gave low *R*-factors. When the Sr^{2+} substitution amounts are 0, 0.5 and 1 for the CSSPO:Eu^{2+}, the refined results are depicted in Fig. 2 as representatives. The observed, calculated, difference, background and Bragg positions are all shown in Fig. 2(a)–(c). According to the refinement results in Fig. 2(d) and Table 1, the lattice parameters *a*, *b* and *c*, and the cell volume (*V*) follow a typical linear increase that depends on the increase of the Sr^{2+} substitution amount *x*, which is in good agreement with the well-known fact that Sr^{2+} ions have larger ionic radii than Ca^{2+} ions. Therefore, we can conclude that the real Ca/Sr ratios of the samples are close to one. The results obey Vegard's rule, which indicates that the Sr^{2+} ions have definitely entered the crystal lattice and replaced the Ca^{2+} ions.[31]

The refinement results of other Sr^{2+} substitution contents are shown in Fig. S1 (ESI†). In terms of the Sc_2O_3 and $Sr_3(PO_4)_2$ impurities, their trace amounts were also analyzed and summarized in Fig. S1 (ESI†). On the basis of the previous reports,[32,33] the emission peaks are located at 403 nm and 484 nm for Sc_2O_3:Eu^{2+} and $Sr_3(PO_4)_2$:Eu^{2+} phosphors, respectively. However, we have confirmed that the minor impurity in the CSSPO:Eu^{2+} samples (x = 0.1–0.9) is Sc_2O_3, and the emission spectra of these samples do not show any emission around 403 nm, reflecting that the Sc_2O_3 has little influence on the emission properties and it can be reasonably ignored. On the other hand, $Sr_3(PO_4)_2$ only exists in the sample when x = 1, and the emission peak is at 525 nm. Similarly, $Sr_3(PO_4)_2$ and CSSPO have no overlapped emission spectra, and the emission of $Sr_3(PO_4)_2$ does not appear in the emission spectra of the samples. In this paper, the major discussion is the series variation by crystal regulation. Therefore, these effect-free minor impurities coming from high accuracy refinements are not discussed. The other refinement information is listed in Table S1 (ESI†), and the fractional atomic coordinates and isotropic displacement parameters of CSSPO:Eu^{2+} (x = 0–1) are listed in Table S2 in the ESI.†

To elucidate the complex crystal structure based on the refinement result, Fig. 3(a) illustrates the schematic of the CSSPO crystal structure and the coordination environment. The as-prepared CSSPO possess the same crystal structure as the CSPO host, which crystallizes in a rhombohedral cell (space group *R3c*, no. 161, Z = 6). Several crystallographically independent cation sites in the unit cell are determined as follows: Ca^{2+} ions have three kinds of sites and they locate in the eight-coordinated O^{2-} environments. The three kinds of polyhedrons connect with each other *via* sharing the same vertexes and faces. Sc^{3+} ions are six-coordinated, and there are three kinds of P^{5+} sites, with each P^{5+} ion coordinating with four O^{2-} ions to form a tetrahedron. In addition, the effective radii of the Ca^{2+}, Eu^{2+} and Mn^{2+} ions are 1.12 Å, 1.25 Å and 0.96 Å in the 8-coordinated environment, respectively. In view of the similar ionic radii and the charge balance, it is reasonable to infer that Eu^{2+} and Mn^{2+} will randomly occupy the three Ca^{2+} sites in the host structure. Fig. 3(b) shows that the average bond lengths d(Ca/Sr–O) follow a linear tendency with Sr^{2+} substitution. Although the Ca/Sr ratio value was not refined for the Ca1/Sr1, Ca2/Sr2, and Ca3/Sr3 sites (Fig. 3a), linear behavior of their average bond lengths, d(Ca/Sr–O) (Fig. 3(b)), agrees well with the suggestion that all of the Ca^{2+} sites are almost equally occupied by Sr^{2+} ions. This is strong evidence to verify the lattice expansion due to structural adjustment, and that all Sr/Ca sites are randomly occupied by Sr/Ca.

Fig. 4(a)–(c) illustrate the HRTEM images for the representative CSSPO:Eu^{2+} (x = 0, 0.5, and 1) samples, respectively. Obviously, the studied samples present clear lattice stripes in the selected area, indicating the good crystallinity without apparent defects. It is worth mentioning that the nanosegregation could also be captured by the HRTEM images. In Fig. 4(a) and (c), when x = 0 and x = 1, the distinct lattice fringes uniformly distribute with a large scale in

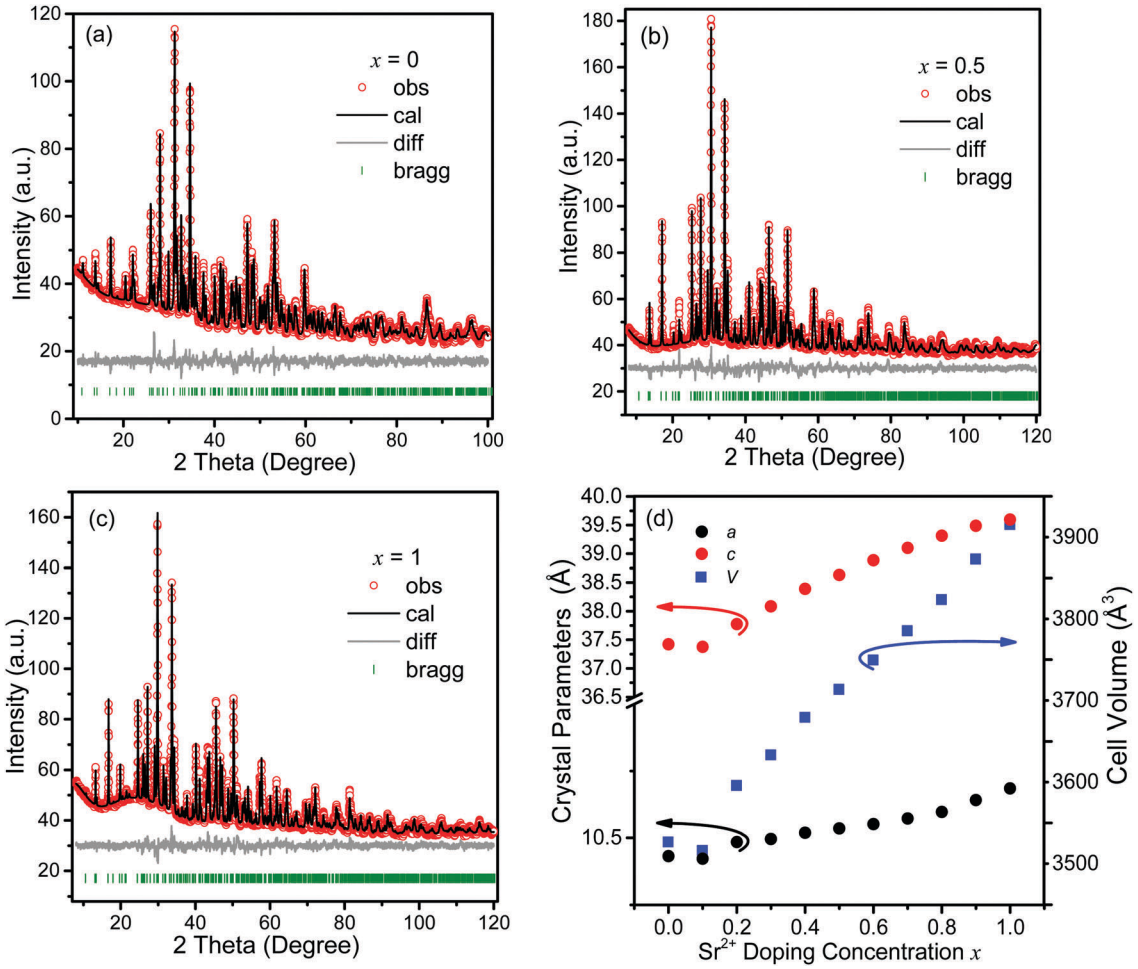

Fig. 2 The Rietveld refinements of the CSSPO:xEu^{2+} phosphors: (a) x = 0, (b) x = 0.5, and (c) x = 1. The green vertical lines represent the position of the Bragg reflection. The grey lines represent differences between the calculated (black lines) and observed (circle symbols) results. (d) is the relation between the Sr^{2+} cation substitution amount and the lattice parameters a(b) and c, as well as the crystal lattice volumes obtained from the Rietveld refinements.

Table 1 The main parameters of the processing and refinement of the CSSPO:Eu^{2+} (x = 0–1) samples

x	0	0.5	1
a	10.432(5)	10.535(5)	10.685(3)
b	10.432(5)	10.535(5)	10.685(3)
c	37.422(2)	38.633(2)	39.597(1)
V	3526.7(6)	3713.4(4)	3915.3(3)
R_{wp}	5.80	5.28	4.25
R_p	4.22	3.89	3.19
R_B	1.91	2.31	1.86
χ^2	3.18	2.78	2.92

the HRTEM images. However, there are many small range lattice fringes with different orientations when x = 0.5, and this suggests the appearance of nanosegregation in the studied systems. With the purpose of confirming this deduction, we measured the interplanar distances with all different orientations. By comparing them, we found that both lattice fringes corresponding to (3 0 0) and (0 2 10) exist in Fig. 4(b). This means that the similar microstructures that belong to the samples of both x = 0 and x = 1 simultaneously exist in the sample of x = 0.5.

Furthermore, when observing the crystallographic planes in different orientations assigned to different indices of the crystal plane, we could utilize the interplanar distance (d-spacing) equation for hexagonal systems:

$$d = \frac{a}{\sqrt{\frac{4}{3}(h^2 + k^2 + hk) + l^2\frac{a^2}{c^2}}}$$

to transfer the values of different interplanar distances into distances with the same indices of the crystal plane. Through comparing the d-spacings that belong to the same crystal plane, the crystal structure variation with the substitution content of Sr^{2+} ions could be reflected. As shown in Fig. 4(a) and (b), 0.2839 nm and 0.2846 nm correspond to the (0 2 10) plane. By the calculation of transforming the (3 0 0) plane into (0 2 10) in Fig. 4(c), the d-spacing value of 0.2857 nm is determined to correspond to the (0 2 10) plane. The continuous increase in the d-spacing values reflects the lattice variation with the doping of Sr^{2+} ions. This result further confirms the successful

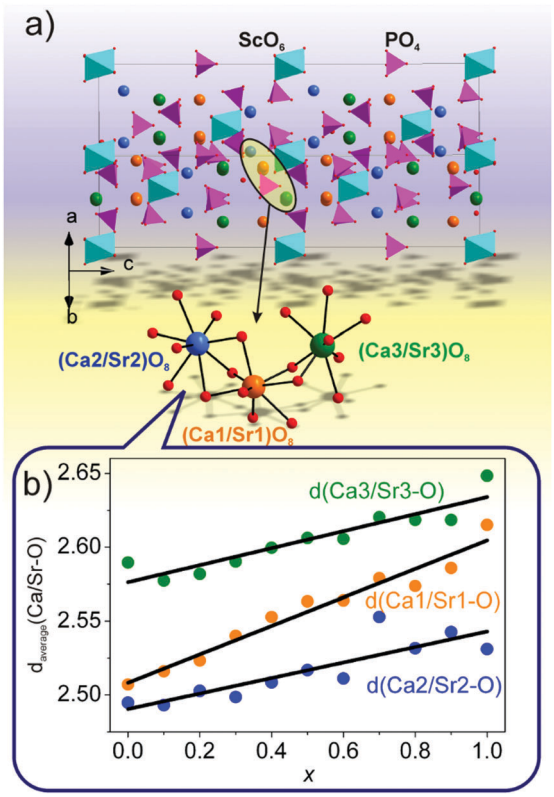

Fig. 3 (a) The schematic crystal structure of CSSPO, showing the polyhedra of ScO_6 and PO_4; the inset is a diagram of the three kinds of Ca sites that can be occupied by Eu^{2+} and Mn^{2+}. (b) The linear graph of the average bond length d(Ca/Sr–O) variations depending on the Sr^{2+} doping concentration.

replacement of Ca^{2+} ions by Sr^{2+} ions and the formation of a solid solution phase.

3.2 Photoluminescence and energy transfer properties of the phosphor

In order to investigate the effect of structural variation in the solid solution phase on the luminescence of the studied samples, the Eu^{2+} doping concentration for all the of samples discussed later is set as 3%. Fig. 5(a) and (b) show the PLE and PL spectra of the CSSPO:Eu^{2+} recorded at room temperature, respectively. The excitation spectra show a broad absorption band in the range from 200 to 450 nm when fixing the emission wavelength at the peak position. Under the optimum excitation wavelength of 368 nm, the CSPO:Eu^{2+} shows the characteristic $4f^6 5d \rightarrow 4f^7$ transition emission of Eu^{2+} ions peaking at 485 nm.[34]

To expound the effect of structural evolution on the luminescence with increasing Sr^{2+} concentration (x) in CSSPO:Eu^{2+}, the emission spectra were further characterized. As shown in Fig. 5(b), the normalized emission spectra exhibit a gradual red-shift with increasing x under 368 nm ultraviolet excitation. The corresponding emission peaks shift from 483 nm to 525 nm until the complete replacement of Ca^{2+} ions by Sr^{2+} ions. This result reveals that the formation of a solid solution influences the coordination environment surrounding the Eu^{2+} ions, and finally results in a spectral shift. Furthermore, it is worth mentioning that the emission shape changes with the substitution process. Actually, the emission spectra are the combined results of the emission bands corresponding to the three luminescent centers, and all of these sites are influenced by the crystal field strength. As shown in Fig. 3(b), with the substitution process, the three Ca–O bond lengths have different levels of expansion. Therefore, the crystal field strengths of the three sites exhibit different levels of variation. This directly leads to the relative intensity variation of the three sub-bands. Consequently, the shapes of the emission spectra change with the substitution process. Besides the spectral change, the $Sr^{2+} \rightarrow Ca^{2+}$ cation substitution also affects the emission intensity of Eu^{2+} ions in the CSSPO:Eu^{2+} system. As shown in Fig. 5(c), the integrated emission intensity constantly increases with increasing values of x, which should come from the continuous change in lattice rigidity and distortion due to the radius mismatch of Ca^{2+} ions and Sr^{2+} ions. Fig. 6 presents the color coordinates evolution trend of the CSSPO:Eu^{2+} with x on the CIE diagram depicted by the black arrow. Clearly, the color coordinates of the studied samples display an approximately linear evolution, further confirming the controllable luminescence tuning based on the $Sr^{2+} \rightarrow Ca^{2+}$ cation substitution method. Correspondingly, under 365 nm UV lamp illumination, the emission colors of the CSSPO:Eu^{2+} phosphors could

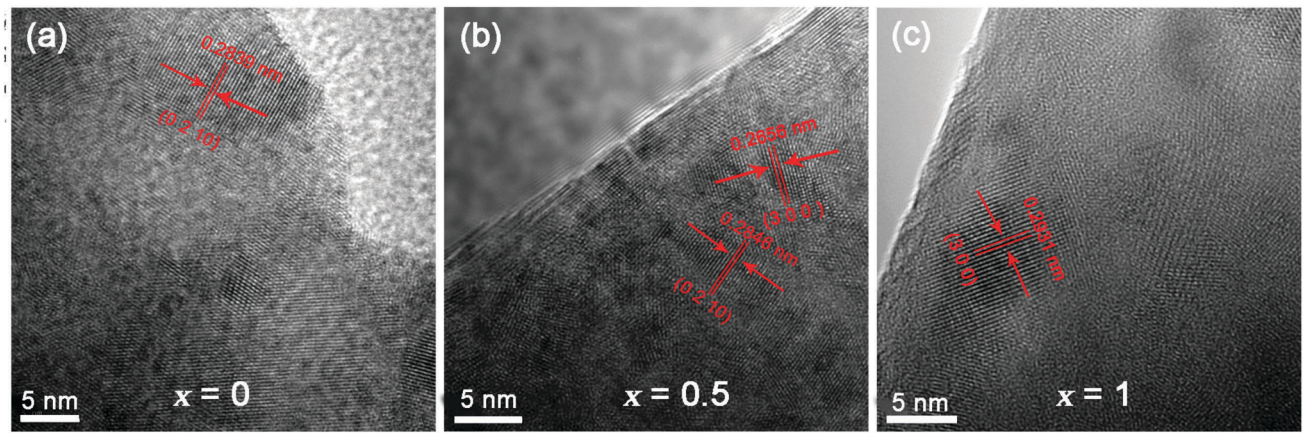

Fig. 4 The HRTEM images of the samples CSSPO:Eu^{2+} for the x = 0, 0.5, and 1, respectively.

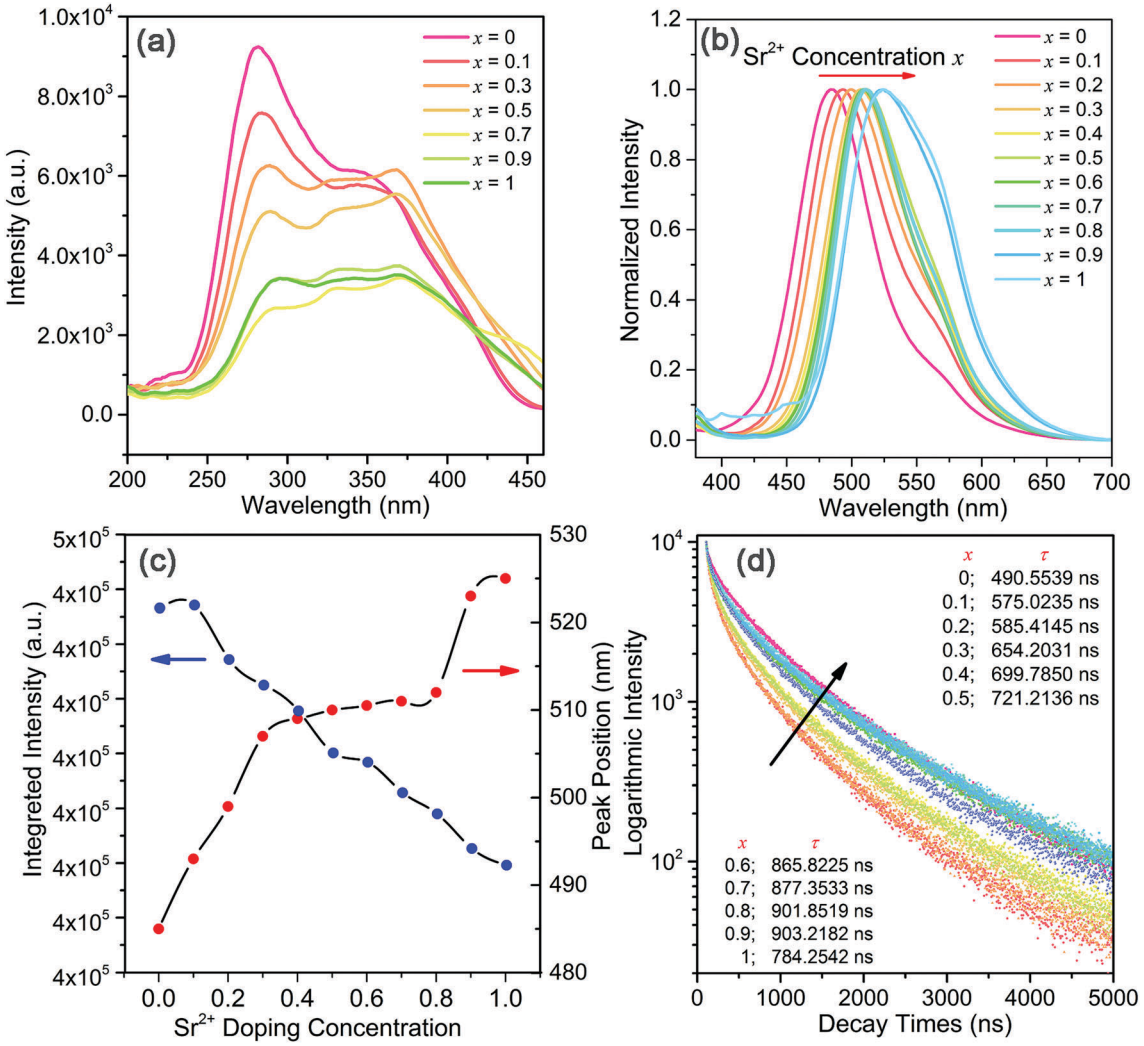

Fig. 5 Photoluminescence (a) excitation (λ_{em} = 484–524 nm) and (b) emission (λ_{ex} = 368 nm) spectra of the CSSPO:Eu^{2+} samples with different Sr^{2+} doping concentrations. (c) The changes in the integrated emission intensity and the wavelengths of the emission peaks depending on the Sr^{2+} substitution amount. (d) The corresponding decay curves of the CSSPO:Eu^{2+} samples with different Sr^{2+} doping concentrations; the specific values of the lifetimes are given in the inset.

continuously change from blue to yellow, as shown by the luminescence photos in Fig. 7. Herein, we infer that the constant red-shift behaviors are associated with the liner structure variation induced by the solid solution phase transformation.

According to the previous reports about the luminescence tuning induced by cation substitution,[31,35–44] the red-shift mechanism mainly results from several possible factors: the polarizability of the anions in the first coordination sphere, the crystal field strength and covalency (the nephelauxetic effect). However, in this work, the polarizability of the anions in the first coordination remains unchanged with Sr^{2+} substitution, so the red-shift in emission cannot be ascribed to this. Therefore, we aspire to clarify the mechanism considering the two factors of crystal field strength and covalency.

As mentioned in the structural analysis of the CSPO host, three kinds of CaO_8 polyhedra are connected in sequence, which are suitable for Eu^{2+} doping. Considering the sensitivity of Eu^{2+} ions to the crystal field environment, the cation substitution of Sr^{2+} for Ca^{2+} will directly influence the luminescence property.[45] $Eu_9Sc(PO_4)_7$ is isotypic to $Ca_9Sc(PO_4)_7$, and thus $(Eu/Ca)_9Sc(PO_4)_7$ can form a complete solid solution due to the similar ion radii of Eu^{2+} (r = 1.25 Å, CN = 8) and Ca^{2+} (r = 1.12 Å, CN = 8).[46] Therefore, the doped Eu^{2+} ions will enter into the Ca^{2+} sites in the $Ca_9Sc(PO_4)_7$ lattice to form luminescence centers. When Ca^{2+} ions are exchanged by Sr^{2+} ions, the Sr^{2+} ions randomly occupy the Ca^{2+} sites, including the neighboring Ca^{2+} sites around the Eu^{2+} ions. The structural variation caused by cation substitution around the luminescent centers will definitely influence the crystal field strength. According to the refinement analysis, it is found that the average Eu/Ca–O bond length constantly increases with Sr^{2+} doping, as indicated in Fig. 3(b). Commonly, the crystal field strength can be estimated using the equation:[47]

$$D_q = \frac{Ze^2r^4}{6R^5}$$

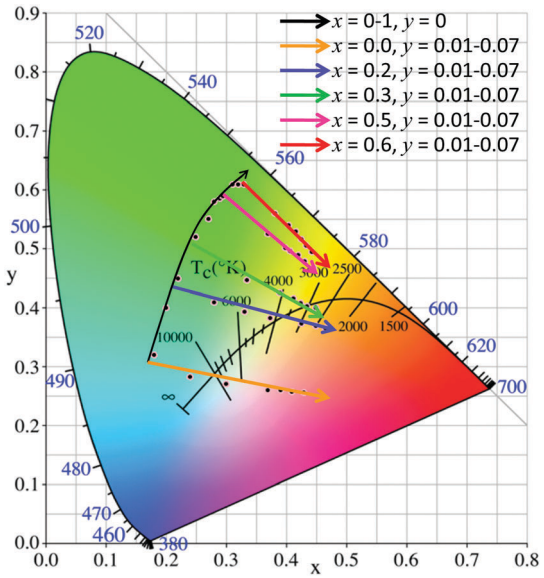

Fig. 6 The color coordinates of the phosphors CSSPO:Eu^{2+} (x = 0–1) and CSSPO:Eu^{2+},Mn^{2+} (x = 0, 0.2, 0.3, 0.5, and 0.6; y = 0.01–0.07) are shown as the black dots. Different color arrows represent the CCT change trends with the Sr^{2+} and Mn^{2+} doping concentration, and the corresponding ranges of x and y are shown as insets.

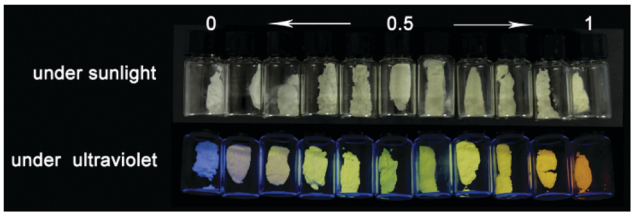

Fig. 7 Photographs of the CSSPO:Eu^{2+} (x = 0–1) phosphors under UV light and natural light.

where Z is the charge or valence of the anion, e is the charge of an electron, r is the radius of the d wave function and R is the distance between the central ion and its ligands. For the particular system CSSPO:Eu^{2+}, Z, e and r are constants, and Dq is inversely proportional to R^5. As demonstrated in Fig. 8, the increasing average bond lengths easily result in the gradually decreasing crystal field strength with x. This result appears to contradict with the experimental result of the emission wavelength red-shift. Actually, besides the distance R, the symmetry of the Eu^{2+} sites also exerts an important impact on the crystal field strength. The introduction of Sr^{2+} ions usually decreases the symmetry of the original crystal structure, and thus it will strengthen the crystal field splitting and preferential orientation of the Eu^{2+} d orbit. The polyhedron distortion index, which evaluates the symmetry of the crystal structure, can be calculated using the following equation:[48]

$$D = \frac{1}{n}\sum_{i=1}^{n}\frac{|l_i - l_{av}|}{l_{av}}$$

where l_i is the distance from the central atom to the ith coordinating atom and l_{av} is the average bond length. When increasing the Sr^{2+} content, the distortion indexes increase as

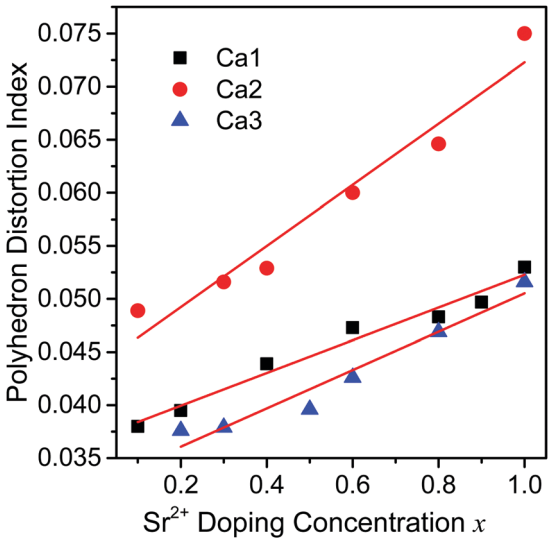

Fig. 8 Variation of the polyhedron distortion indexes of Ca1, Ca2, and Ca3 sites with Sr^{2+} substitution amount.

demonstrated in Fig. 8. As a result, the determinant factors of the crystal field strength become complex, and should be the result of two competing effects. Finally, the lattice distortions generate a bigger effect, which accordingly leads to the emission peaks moving to a longer wavelength.

With respect to other factors, it is well known that the covalency between the Eu^{2+} ions and ligands in the host lattice is not only relevant to the distance, but also associated with the metal ions in the neighborhood.[49] The electronegativity of the metal ions could be used to evaluate the ability of attracting electrons.

In the studied system, the electronegativity will decrease on substituting Sr^{2+} for Ca^{2+}. In terms of the competition between the Eu–O bond and its neighboring Sr–O bond, the decreasing attraction of Sr^{2+} ions means that the Eu–O bond becomes tenser and shorter. This enhances the covalency around the Eu^{2+} ions. This result reduces the nephelauxetic effect of the Eu^{2+} 5d energy levels in the CSSPO:Eu^{2+} series and thus drives the emission wavelengths to shift in the lower energy direction. From the mechanisms described above, it is reasonable that a red-shift occurred with increasing Sr^{2+} concentration.

Inspired by the linear evolution of the lattice parameters obtained from the refinement results, we aspired to verify the existence of nanosegregation in this system based on the emission spectra. In the equation $I(x) = C[xI(\mathrm{SSPO}) + (1 - x)I(\mathrm{CSPO})]$,[26] CSPO and SSPO represent CSSPO:Eu^{2+} when x = 0 and x = 1, respectively. If the emission spectra could satisfy this relation, then phase nanosegregation quite possibly occurred. Based on the integrated emission intensity as show in Fig. 5(c), the emission intensity values of all the samples show a linear relation with the substitution concentration. Except for the samples x = 0.1 and x = 0.5, which have minor deviation, the rest of the samples all show a good fitting with the equation mention above. This consistency between linear evolution of the structure and optical spectroscopy clearly proves the existence of the segregation in the nanoscale region in the host lattice.

That is to say, the nanosegregation could give rise to a tunable photoluminescence property without disorder of the long-range structure and phase emerging. Meanwhile, it explains the possibility of complete replacement of Sr^{2+} with Ca^{2+} without impurities.

As essential parameters of the luminescence properties, lifetimes are meaningful to reflect the structure variation evolution and environment of the luminescent activator. Fig. 5(d) shows the decay curves of the CSSPO:Eu^{2+} phosphors as a function of the Sr^{2+} substitution amount x, and the lifetimes are all calculated as shown in Fig. 5(d). All of the decay curves obey the triple-exponential fitting according to the equation:[50]

$$I_t = I_0 + A_1 \exp\left(\frac{-t}{\tau_1}\right) + A_2 \exp\left(\frac{-t}{\tau_2}\right) + A_3 \exp\left(\frac{-t}{\tau_3}\right)$$

And the effective lifetime constants can be expressed as:[50]

$$\tau^* = \left(A_1\tau_1^2\right) + A_2\tau_2^2 + A_3\tau_3^2/\left(A_1\tau_1 + A_2\tau_2 + A_3\tau_3\right)$$

where I_t is the luminescence intensity, A_1, A_2 and A_3 represent the fitting constants, t is the time, and τ_1, τ_2 and τ_3 stand for the three different lifetimes for the exponential components. Typically, the three different lifetimes τ_1, τ_2 and τ_3 coincide with the three kinds of sites[36] that could be entered by Eu^{2+} in this host, but limited by the practical experimental conditions, the three lifetimes cannot be distinguished to assign the three specific Ca sites mentioned above.[37,51] Utilizing the effective lifetimes τ^* calculated above, the lifetimes increase with increasing Sr^{2+} substitution concentration, except for the sample in which the Ca^{2+} ions are all replaced by Sr^{2+}. The correlation between the red-shift phenomenon and the lifetime increase could be explained as follows: the red-shift means the emission spectra move in the lower energy direction and this directly slows down the rates of the excitons transition from the excited level back to the ground state. Consequently, the decay rates of the emission get slower and the lifetimes of the phosphor increase.

For the purpose of achieving the final two-dimensional tuning of the color coordinates, the energy transfers from the Eu^{2+} ions to Mn^{2+} ions were introduced, except for the above crystal field regulation. Taking advantage of the $Eu^{2+} \rightarrow Mn^{2+}$ energy transfer, the final white emission was obtained in the CSSPO:Eu^{2+},Mn^{2+} system. The emission spectra of the representative CSSPO:0.27Eu^{2+},9$y$$Mn^{2+}$ samples with x = 0, 0.2, 0.3, 0.5, and 0.6, and y = 0.01–0.07 are shown in Fig. S2 (ESI†). Obviously, the emission intensities of the Mn^{2+} ions all appear to increase, while the Eu^{2+} emission intensities gradually decrease with increasing Mn^{2+} content, confirming the occurrence of an energy transfer process. As a result, the simultaneous tuning of the emission wavelengths and intensities of the Eu^{2+} and Mn^{2+} ions could be accurately achieved, and the two-dimensional tuning of the color coordinates could be realized. Fig. 9 presents the luminescence digital photographs of the CSSPO:Eu^{2+},Mn^{2+} phosphors under the excitation of 365 nm UV light within the limitation of x = 0, 0.2, 0.3, 0.5 and 0.6 and y = 0.01–0.07. The changing trend of the luminous color agrees with that of the color coordinates on the CIE diagram, as shown in Fig. 6. This result confirms our expectation: crystal field regulation and energy transfer can efficiently and controllably adjust the luminescence properties of the phosphors without obvious mutual interference.

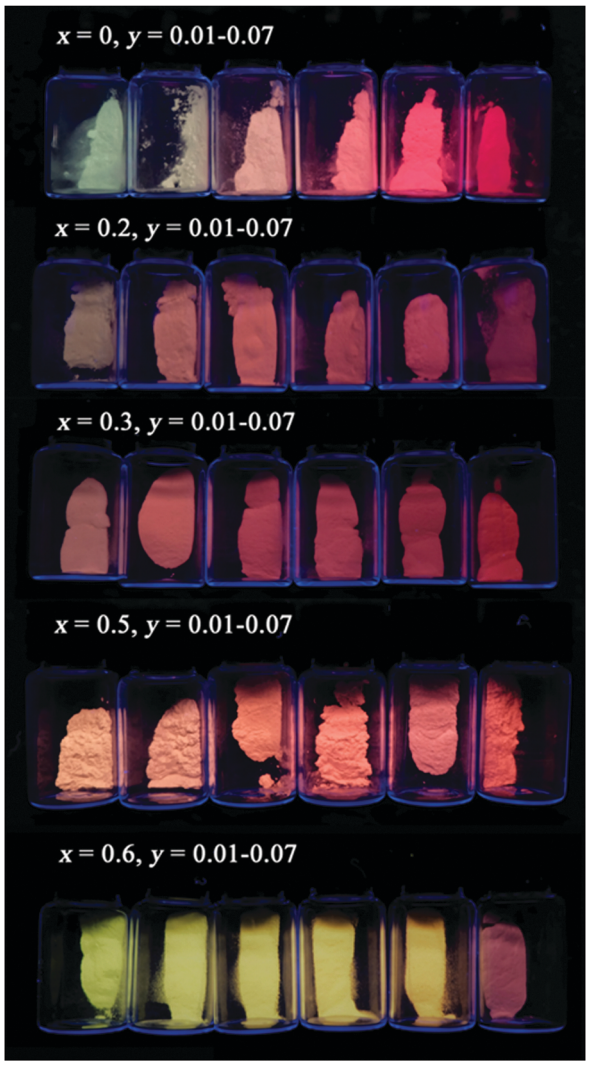

Fig. 9 The emission color photographs of the phosphors CSSPO: Eu^{2+},Mn^{2+} with the limitation of x = 0–0.6 and y = 0.01–0.07.

As an important parameter for evaluating the energy transfer process, the energy transfer efficiency from Eu^{2+} to Mn^{2+} in the CSSPO:Eu^{2+},Mn^{2+} system could be calculated using the equation as follows:[52]

$$\eta_T = 1 - \frac{\tau_S}{\tau_{S0}}$$

τ_S and τ_{S0} are the lifetimes of Eu^{2+} in the presence and absence of Mn^{2+} ions, respectively. The decay curves of the CSSPO:Eu^{2+},Mn^{2+} phosphors are all shown in Fig. S3 (ESI†). The lifetimes are calculated and listed in Table S3 (ESI†). When x = 0.2, 0.3, 0.5, and 0.6, the energy transfer efficiencies were calculated as a function of the Mn^{2+} concentration and the results are illustrated in Fig. 10. It is observed that the values of the energy transfer efficiencies increase with increasing Mn^{2+} doping concentration. The maximum value of the efficiency could reach 96%, confirming the highly efficient energy transfer between Eu^{2+} and Mn^{2+} in the CSSPO host.

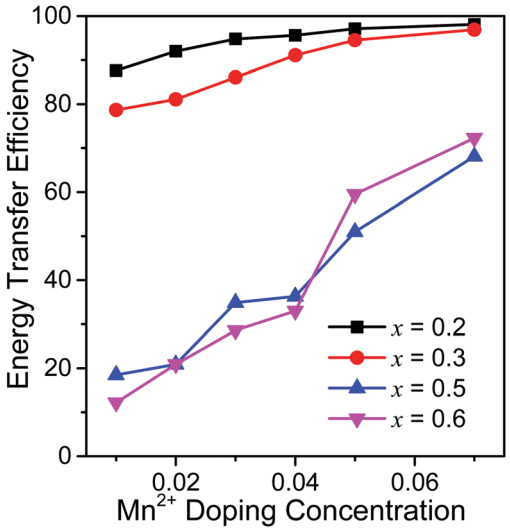

Fig. 10 The relation of the energy transfer efficiencies with the Mn^{2+} doping concentration under excitation at 368 nm.

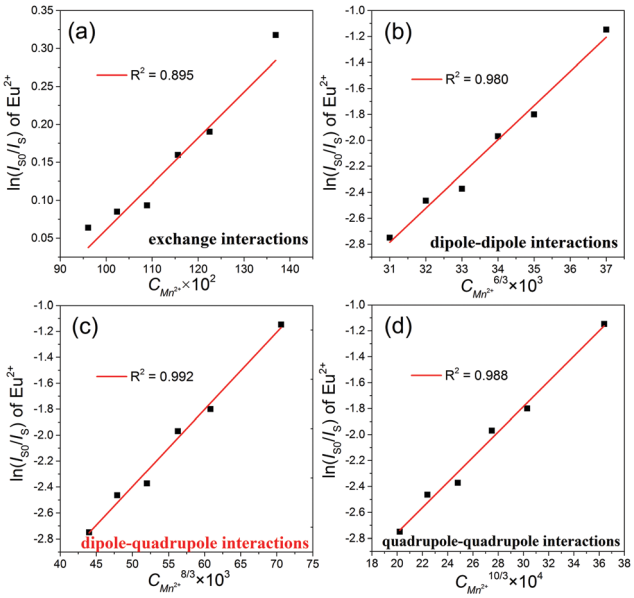

Fig. 11 Dependence of (a) $\ln(I_{S0}/I_S)$ of Eu^{2+} on $C_{Mn^{2+}}$; and I_{S0}/I_S of Eu^{2+} on (b) $C_{Mn^{2+}}{}^{6/3}$; (c) $C_{Mn^{2+}}{}^{8/3}$ and (d) $C_{Mn^{2+}}{}^{10/3}$.

The energy transfer mechanisms could be investigated by calculating the critical distance R_{Eu-Mn} as depicted in the equation:[53,54]

$$R_{Eu-Mn} = 2\left(\frac{3V}{4\pi x_C Z}\right)^{\frac{1}{3}}$$

Thereinto, V is the volume of the crystal cell, x_C is the total doping concentration when the energy transfer efficiency is 0.5, and Z is the number of cation sites that can be occupied by activator ions. The critical distance R_{Eu-Mn} is 17.78 Å without Sr^{2+} substitution. Furthermore, the cell volume continuously increases with the x value. Therefore, the R_{Eu-Mn} values of the CSSPO:Eu^{2+},Mn^{2+} samples are absolutely larger than 5 Å, which is defined as the exchange interaction. It is reasonable to assign the energy transfer mechanism as the electric multipolar interaction.

Based on Dexter's energy transfer formula of multipolar interaction and Reisfeld's approximation:[53,54]

$$\frac{\eta_0}{\eta} \propto C^{\frac{\alpha}{3}}$$

where η_0 and η are the luminescence quantum efficiencies of Eu^{2+} in the absence and presence of Mn^{2+}, respectively; C is the sum of the concentration of Eu^{2+} and Mn^{2+} ions; and α values of 3, 6, 8, and 10 correspond to exchange, dipole–dipole, dipole–quadrupole, and quadrupole–quadrupole interactions, respectively. The value of η could also be obtained by approximately calculating the ratio of the related luminescence intensities as:

$$\ln\left(\frac{I_{S0}}{I}\right) \propto C$$

$$\frac{I_{S0}}{I_S} \propto C^{\frac{\alpha}{3}}$$

where I_{S0} and I are the luminescence intensity of Eu^{2+} in the presence and absence of Mn^{2+}. The plot is shown in Fig. 11, which is fitted with α = 3, 6, 8, and 10, respectively. The fitting parameter R^2, which is regularly used to evaluate the linear fitness, gives the maximum value α = 8, indicating that the energy transfer from Eu^{2+} to Mn^{2+} is a dipole–quadrupole interaction.

3.3 Thermal stability and application in white LEDs

During practical application in w-LEDs, the employed phosphors need to work in a high-power environment where the joint-temperature of the LED chips could reach 150 °C. Hence, the temperature-dependent photoluminescence properties are essential to evaluate the performance of a phosphor. The PL spectra of the measured samples with Sr^{2+} doping concentrations of x = 0, 0.3, 0.5, 0.8 and 1 were all collected from 0 °C to 200 °C, recorded at a temperature interval of 25 °C, and Fig. 12(a)–(c) are the representative temperature-dependent PL spectra of CSSPO:Eu^{2+} (x = 0, 0.5, and 1), respectively. The observed slight blue shift of the emission peaks could be attributed to thermally active phonon-assisted tunneling.[39] Due to the thermal quenching,[55] the PL intensity of all of the CSSPO:Eu^{2+} (x = 0–1) phosphors decreases with the increase in temperature. At 150 °C, the emission intensity of Eu^{2+} could remain at 71% to 47% of the initial intensity at room temperature for the five samples, as shown in Fig. 12(d). The reason for the thermal quenching is shown in Fig. 12(e): the electrons that absorb excitation energy will transition from the ground state $4f^7$ to the excited states $5d4f^6$. Normally, the excited electrons undergo radiative relaxation and return to the ground state directly with light emission. However, apart from the radiative relaxation, non-radiative relaxation occurs at the same time when the phosphor is under high-temperature thermal activation. The excited electrons will reach the crossing point, C, of the ground state and excited state, and then go back to the ground state directly without luminescence emission, which leads to thermal quenching.[56,57] Furthermore, in terms of the emission of Eu^{2+}, different degrees of thermal quenching

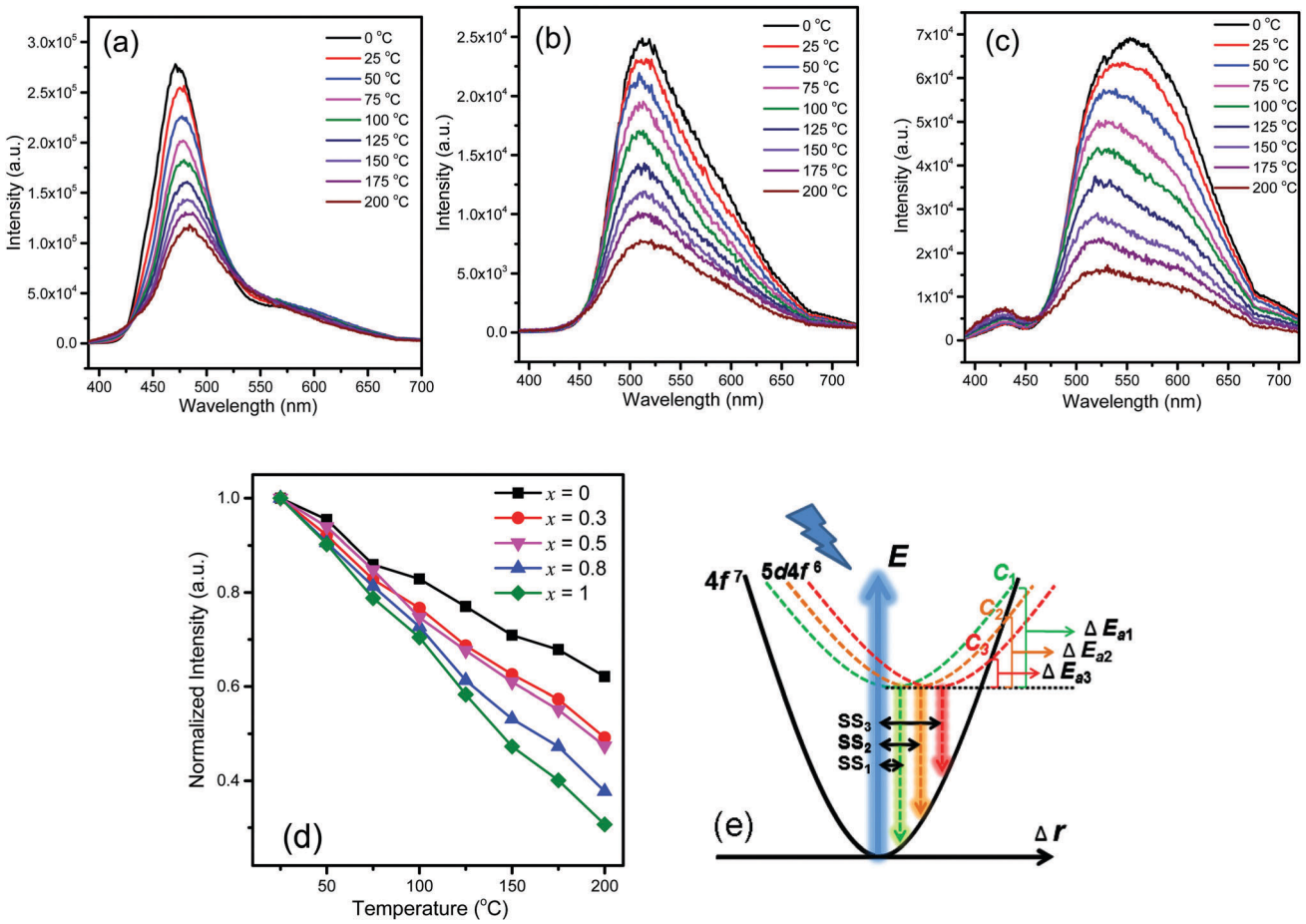

Fig. 12 (a–c) The temperature dependent spectra of the CSSPO:Eu^{2+} (x = 0, 0.5 and 1) phosphors under excitation at 368 nm, respectively. (d) The linear diagram of the normalized intensity of the CSSPO:Eu^{2+} (x = 0, 0.3, 0.5, 0.8, and 1) phosphors at different temperatures. (e) The configurational coordinated diagram of the Eu^{2+} in CSSPO:Eu^{2+} and the activation energy change trends with the emission spectra red shift.

are associated with the Sr^{2+} doping concentration, which is observed from the results. This is because when the Sr^{2+} doping concentration increases, the emission spectra exhibit a continuous red-shift, which also means that the Stokes shift increases. The Stokes shift dominates the location of the point C as shown in the figure, and it could be concluded that the thermal activation energy decreases on increasing the Sr^{2+} doping concentration in this system. The activation energy could be calculated using the equation $I_T = I_0\left[1 + c\exp\left(-\frac{\Delta E}{KT}\right)\right]^{-1}$,[58,59] where K is the Boltzmann constant. For x = 0, 0.3, 0.5, 0.8, and 1, the values of the activation energy are 0.236, 0.205, 0.203, 0.188, and 0.171 eV, respectively. This result coincides with the discussion of the configurational coordinated diagram, where the activation energy decreases with the emission spectra red-shift.

Finally, the electro-luminescence performance of the as-prepared CSSPO:Eu^{2+},Mn^{2+} phosphors was evaluated by coating them onto 369 nm UV LED chips. In order to prepare the ideal indoor lighting source, several white-emitting CSSPO:Eu^{2+},Mn^{2+} phosphors were selected to fabricated w-LED devices. Moreover, the CSSPO:Eu^{2+} (x = 0 and 1) phosphors were also used for comparison. Based on the commercial standard of warm white light,[60] the optimum performance appears for the x = 0.5, y = 0.02 and x = 0.6, y = 0.02 samples. Their EL spectra, luminescence photographs and relevant parameters are all illustrated in Fig. 13. With different compositions of the phosphors under 20 mA current, the CRI changed from 66 to 85, and the CCT is around 3000 K. The emission spectrum ranges from 400 nm to 780 nm, and the wavelength scope exactly covers the entire visible light region to achieve full spectrum lighting.[61,62] The CRI, CCT and color coordinates are indicated in the insets of the figure. Moreover, the color coordinates of the as-prepared w-LED devices all locate in the warm white light region. Accordingly, the emission spectra of the above w-LED devices ranging from 400 nm to 780 nm exactly cover the entire visible light region to finally achieve a full spectrum white lighting source.[63] The $R9$ value can be used to evaluate the red light component in w-LEDs. Typically, a higher $R9$ value reflects a lower color temperature. For the samples with the different CSSPO:Eu^{2+} phosphors, the $R9$ values are 57.8, 86.2, 89.0 and 75.3 for the four w-LEDs in Fig. 13(a)–(d), respectively. As for the luminescence efficiency, the results are 44.42, 53.88, 71.0 and 51.86 lm W^{-1} for the w-LED samples in Fig. 13(a)–(d), respectively.

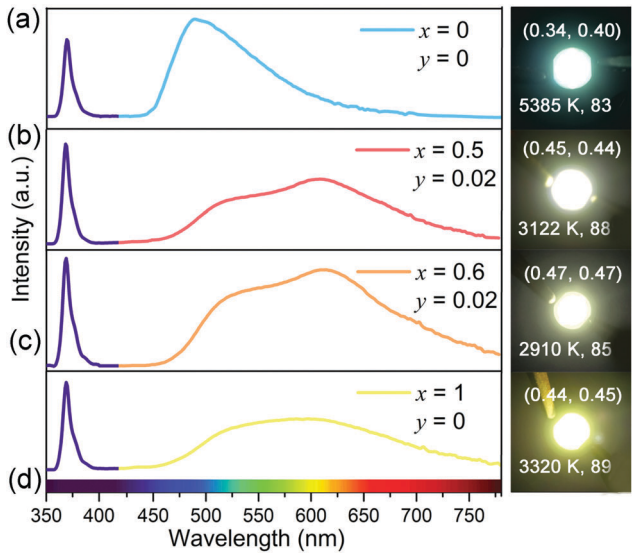

Fig. 13 The EL emission spectra and the corresponding emission photographs for the composites of 369 nm UV chips and the CSSPO:Eu^{2+},Mn^{2+} white emitting phosphors. The insets of the photos are the color coordinates, CRI and CCT, respectively.

4. Conclusions

In this work, a series of $Ca_{9(1-0.03-x-y)}Sr_{9x}Sc(PO_4)_7$:0.27$Eu^{2+}$,9y$Mn^{2+}$ phosphors have been successfully synthesized by a solid-state method. The introduction of Sr^{2+} and Mn^{2+} ions has few effects on the crystal structure of the host lattice due to the formation of a solid solution phase. By combining crystal field regulation and energy transfer, the two-dimensional tuning of the emission colors on the CIE diagram has been achieved. The Rietveld refinements confirmed the effect of cation substitution on the luminescence properties by analyzing the variation in the bond length and crystal lattice parameters. In addition, the appearance of nanosegregation is confirmed and investigated using TEM and photoluminescence emission spectra. The $Eu^{2+} \rightarrow Mn^{2+}$ energy transfer mechanism is also determined to be dipole–quadrupole interaction. The excellent luminescence performance of the w-LEDs fabricated from UV chips and single-component CSSPO:Eu^{2+},Mn^{2+} white phosphors suggests that the design of the two-step tuning method is effective and feasible. Although some luminescence properties need further promotion, this method combining energy transfer and crystal field regulation still has the potential to be applied to other phosphor systems to obtain perfect single-component white-emitting phosphors for utilization in indoor lighting.

Conflicts of interest

There are no conflicts to declare.

Acknowledgements

This work was financially supported by the National Natural Science Foundation of China (NSFC No. 51672265, 51672266, 21521092, 51750110511, 51672257, and 51672259), the Key Research Program of Frontier Sciences of CAS (Grant No. YZDY-SSW-JSC018), the National Basic Research Program of China (2014CB643803), the Scientific and Technological Department of Jilin Province (Grant No. 20150520029JH and 20170414003GH), Jiangmen Innovative Research Team Program (2017) and Major Program of Basic Research and Applied Research of Guangdong Province (2017KZDXM083), the Russian Science Foundation (Grant No. 17-12-01047), and the Distinguished Scientist Fellowship Program of King Saud University, as well as the Deanship of Scientific Research at King Saud University through research group no. (RG-1939-038).

References

1 A. Kalaji, M. Mikami and A. K. Cheetham, *Chem. Mater.*, 2014, **26**, 3966–3975.
2 S. Li, L. Wang, Q. Zhu, D. Tang, X. Liu, G. Cheng, L. Lu, T. Takeda, N. Hirosaki and Z. Huang, *J. Mater. Chem. C*, 2016, **4**, 11219–11230.
3 S. Liang, M. Shang, H. Lian, K. Li, Y. Zhang and J. Lin, *J. Mater. Chem. C*, 2017, **5**, 2927–2935.
4 C. C. Lin, W.-T. Chen, C.-I. Chu, K.-W. Huang, C.-W. Yeh, B.-M. Cheng and R.-S. Liu, *Light: Sci. Appl.*, 2016, **5**, e16066.
5 L. Wang, R.-J. Xie, T. Suehiro, T. Takeda and N. Hirosaki, *Chem. Rev.*, 2018, **118**, 1951–2009.
6 Q.-Q. Zhu, L. Wang, N. Hirosaki, L. Y. Hao, X. Xu and R.-J. Xie, *Chem. Mater.*, 2016, **28**, 4829–4839.
7 G. Dong, B. Chen, X. Xiao, G. Chai, Q. Liang, M. Peng and J. Qiu, *Nanoscale*, 2012, **4**, 4658–4666.
8 G. Bai, M.-K. Tsang and J. Hao, *Adv. Funct. Mater.*, 2016, **26**, 6330–6350.
9 Y. Chen, F. Pan, M. Wang, X. Zhang, J. Wang, M. Wu and C. Wang, *J. Mater. Chem. C*, 2016, **4**, 2367–2373.
10 N. C. George, K. A. Denault and R. Seshadri, *Annu. Rev. Mater. Res.*, 2013, **43**, 481–501.
11 W. B. Im, S. Brinkley, J. Hu, A. Mikhailovsky, S. P. DenBaars and R. Seshadri, *Chem. Mater.*, 2010, **22**, 2842–2849.
12 X. Zhang, J. Wang, L. Huang, F. Pan, Y. Chen, B. Lei, M. Peng and M. Wu, *ACS Appl. Mater. Interfaces*, 2015, **7**, 10044–10054.
13 M. Shang, S. Liang, N. Qu, H. Lian and J. Lin, *Chem. Mater.*, 2017, **29**, 1813–1829.
14 C. Moderie, S. Van der Maren and M. Dumont, Circadian Phase, *Sleep Med.*, 2017, **34**, 148–155.
15 J. H. Oh, S. J. Yang and Y. R. Do, Healthy, Natural, *Light: Sci. Appl.*, 2014, **3**, e141.
16 S. Liang, M. Shang, H. Lian, K. Li, Y. Zhang and J. Lin, *J. Mater. Chem. C*, 2016, **4**, 6409–6416.
17 W. Li, H. Zhang, S. Chen, Y. Liu, J. Zhuang and B. Lei, *Adv. Opt. Mater.*, 2016, **4**, 427–434.
18 A. K. Vishwakarma, K. Jha, M. Jayasimhadri, B. Sivaiah, B. Gahtori and D. Haranath, *Dalton Trans.*, 2015, **44**, 17166–17174.
19 Y. Liu, G. Liu, J. Wang, X. Dong and W. Yu, *Inorg. Chem.*, 2014, **53**, 11457–11466.
20 J. Wang, H. Lin, Q. Huang, G. Xiao, J. Xu, B. Wang, T. Hu and Y. Wang, *J. Mater. Chem. C*, 2017, **5**, 1789–1797.

21 C.-H. Huang, W.-R. Liu and T.-M. Chen, *J. Phys. Chem. C*, 2010, **114**, 18698–18701.
22 Y. Li, B. Li, C. Ni, S. Yuan, J. Wang, Q. Tang and Q. Su, *Chem. – Asian J.*, 2014, **9**, 494–499.
23 P.-P. Dai, C. Li, X.-T. Zhang, J. Xu, X. Chen, X.-L. Wang, Y. Jia, X. Wang and Y.-C. Liu, *Light: Sci. Appl.*, 2016, **5**, e16024.
24 Y. Zhang, X. Li, K. Li, H. Lian, M. Shang and J. Lin, *J. Mater. Chem. C*, 2015, **3**, 3294–3303.
25 M. Hermus, P.-C. Phan, A. C. Duke and J. Brgoch, *Chem. Mater.*, 2017, **29**(12), 5267–5275.
26 Z. Xia, Y. Zhang, M. S. Molokeev, V. V. Atuchin and Y. Luo, *Sci. Rep.*, 2013, **3**, 3310–3317.
27 Z. Xia, G. Liu, J. Wen, Z. Mei, M. Balasubramanian, M. S. Molokeev, L. Peng, L. Gu, D. J. Miller, Q. Liu and K. R. Poeppelmeier, *J. Am. Chem. Soc.*, 2016, **138**, 1158–1161.
28 R. Gautier, X. Li, Z. Xia and F. Massuyeau, *J. Am. Chem. Soc.*, 2017, **139**, 1436–1439.
29 V. A. Morozov, A. A. Belik, S. Y. Stefanovich, V. V. Grebenev, O. I. Lebedev, G. Van Tendeloo and B. I. Lazoryak, *J. Solid State Chem.*, 2002, **165**, 278–288.
30 L. Jiang, R. Pang, D. Li, W. Sun, Y. Jia, H. Li, J. Fu, C. Li and S. Zhang, *Dalton Trans.*, 2015, **44**, 17241–17250.
31 S. Tamboli, P. D. Bhoyar and S. J. Dhoble, *J. Lumin.*, 2017, **184**, 23–28.
32 Z. Wang, Z. Xia, M. S. Molokeev, V. V. Atuchin and Q. Liu, *Dalton Trans.*, 2014, **43**, 16800–16804.
33 Y. Pan, X. J. Xie, Q. W. Huang, C. Gao, Y. B. Wang, L. X. Wang, B. X. Yang, H. Q. Su, L. Huang and W. Huang, *Adv. Mater.*, 2018, **30**, 1705256.
34 F. Chen, X. M. Yuan, F. Zhang and S. W. Wang, *Opt. Mater.*, 2014, **37**, 65–70.
35 X. Li, J. D. Budai, F. Liu, J. Y. Howe, J. Zhang, X.-J. Wang, Z. Gu, C. Sun, R. S. Meltzer and Z. Pan, *Light: Sci. Appl.*, 2013, **2**, e50.
36 M. Kim, M. Kobayashi, H. Kato, H. Yamane, Y. Sato and M. Kakihana, *Dalton Trans.*, 2015, **44**, 1900–1904.
37 K. A. Denault, J. Brgoch, M. W. Gaultois, A. Mikhailovsky, R. Petry, H. Winkler, S. P. DenBaars and R. Seshadri, *Chem. Mater.*, 2014, **26**, 2275–2282.
38 Y. Xia, J. Chen, Y.-G. Liu, M. S. Molokeev, M. Guan, Z. Huang and M. Fang, *Dalton Trans.*, 2016, **45**, 1007–1015.
39 H. Ji, Z. Huang, Z. Xia, M. S. Molokeev, V. V. Atuchin, M. Fang and Y. Liu, *J. Phys. Chem. C*, 2015, **119**, 2038–2045.
40 Z. Ci, M. Que, Y. Shi, G. Zhu and Y. Wang, *Inorg. Chem.*, 2014, **53**, 2195–2199.
41 Y. Wei, X. Qi, H. Xiao, W. Luo, H. Yao, L. Lv, G. Li and J. Lin, *RSC Adv.*, 2016, **6**, 43771–43779.
42 Y. Wei, C. C. Lin, Z. Quan, M. S. Molokeev, V. V. Atuchin, T.-S. Chan, Y. Liang, J. Lin and G. Li, *RSC Adv.*, 2016, **6**, 57261–57265.
43 G. Li, C. C. Lin, W.-T. Chen, M. S. Molokeev, V. V. Atuchin, C.-Y. Chiang, W. Zhou, C.-W. Wang, W.-H. Li, H.-S. Sheu, T.-S. Chan, C. Ma and R.-S. Liu, *Chem. Mater.*, 2014, **26**, 2991–3001.
44 X. Qin, X. Liu, W. Huang, M. Bettinelli and X. Liu, *Chem. Rev.*, 2017, **117**, 4488–4527.
45 B. Lee, S. Lee, H. G. Jeong and K.-S. Sohn, *ACS Comb. Sci.*, 2011, **13**, 154–158.
46 G. Gao, S. Krolikowski, M. Peng and L. Wondraczek, *J. Lumin.*, 2016, **180**, 234–240.
47 M. Zhang, Z. Xia, M. S. Molokeev, L. Shi and Q. Liu, *J. Mater. Chem. C*, 2016, **4**, 9078–9084.
48 N. Guo, H. You, C. Jia, R. Ouyang and D. Wu, *Dalton Trans.*, 2014, **43**, 12373–12379.
49 W. Baur, *Acta Crystallogr., Sect. B: Struct. Crystallogr. Cryst. Chem.*, 1974, **30**, 1195–1215.
50 Z. Xia, C. Ma, M. S. Molokeev, Q. Liu, K. Rickert and K. R. Poeppelmeier, *J. Am. Chem. Soc.*, 2015, **137**, 12494–12497.
51 D. Schweitzer, L. Deutsch, M. Klemm, S. Jentsch, M. Hammer, S. Peters, J. Haueisen, U. A. Müller and J. Dawczynski, *J. Biomed. Opt.*, 2015, **20**, 061106.
52 L. Wang, X. Wang, T. Takeda, N. Hirosaki, Y.-T. Tsai, R.-S. Liu and R.-J. Xie, *Chem. Mater.*, 2015, **27**, 8457–8466.
53 K. Li, H. Lian, M. Shang and J. Lin, *Dalton Trans.*, 2015, **44**, 20542–20550.
54 D. L. Dexter, *J. Chem. Phys.*, 1953, **21**, 836–850.
55 G. Blasse, *Phys. Lett. A*, 1968, **28**, 444.
56 Y. H. Kim, P. Arunkumar, B. Y. Kim, S. Unithrattil, E. Kim, S.-H. Moon, J. Y. Hyun, K. H. Kim, D. Lee, J.-S. Lee and W. B. Im, *Nat. Mater.*, 2017, **16**, 543–550.
57 Y. Zhang, X. Li, K. Li, H. Lian, M. Shang and J. Lin, *ACS Appl. Mater. Interfaces*, 2015, **7**, 2715–2725.
58 P. Dorenbos, *J. Phys.: Condens. Matter*, 2005, **17**, 8103–8111.
59 X. Min, Z. Huang, M. Fang, Y.-G. Liu, C. Tang and X. Wu, *Inorg. Chem.*, 2014, **53**, 6060–6065.
60 J. Chen, Y.-g. Liu, H. Liu, D. Yang, H. Ding, M. Fang and Z. Huang, *RSC Adv.*, 2014, **4**, 18234–18239.
61 K. T. Kamtekar, A. P. Monkman and M. R. Bryce, *Adv. Mater.*, 2010, **22**, 572–582.
62 D. Nötzold, H. Wulff and G. Herzog, *Phys. Status Solidi B*, 1995, **191**, 21–30.
63 H. Ding, S.-B. Yu, J.-S. Wei and H.-M. Xiong, *ACS Nano*, 2016, **10**, 484–491.